

Vertical hole transport through unipolar InGaN quantum wells and double heterostructures

K. S. Qwah^{1,*}, M. Monavarian^{1,*}, W. Y. Ho¹, Y.-R. Wu² and J. S. Speck¹¹Materials Department, University of California, Santa Barbara, California 93106, USA²Graduate Institute of Photonics and Optoelectronics and Department of Electrical Engineering, National Taiwan University, Taipei City 10617, Taiwan

(Received 13 August 2021; revised 2 November 2021; accepted 28 February 2022; published 19 April 2022)

We report unipolar hole transport through unintentionally doped (UID) c-plane Ga-polar InGaN heterostructures to investigate the impact of alloy disorder on vertical transport. Simulations and experimental investigations were conducted on unipolar InGaN double heterostructures (DHs) and quantum well (QW) test structures by varying thicknesses and the number of QWs. The structures were simulated using one-dimensional (1D) and three-dimensional (3D) algorithms, incorporating the effects of random alloy disorder in the 3D model using the newly developed Localization Landscape theory. The electrical polarization discontinuity between GaN and InGaN results in a significant barrier for vertical carrier transport. Band-diagram and current density-voltage simulations indicate asymmetric polarization barriers to the vertical hole transport for the InGaN DHs. For the QW structures, however, the simulations indicate a symmetric barrier to the hole transport in forward and reverse bias. In the case of the InGaN DH layers, the 3D simulation results indicate a smaller barrier to hole transport compared to 1D simulations. For QW simulations, the barriers were found to be the same in both 1D and 3D simulations. The simulation results are experimentally verified using unipolar *p*-type vertical transport structures, enabled by *n*-to-*p* tunnel junctions to facilitate the current spreading within the bulk material for the mesa structures grown by ammonia-molecular beam epitaxy. The results indicate that increasing the UID In_{0.1}Ga_{0.9}N DH layer thickness from 15 to 30 nm increases the forward bias voltage drop (~ 2 V at 500 A/cm²) more than the reverse bias voltage drop (~ 0.2 V at 500 A/cm²). For the QW structures, increasing the number of QWs from one to three increases the voltage penalty similarly in forward and reverse directions (~ 0.25 V per QW at 500 A/cm²). The results are beneficial in understanding the impact of alloy disorder on the transport properties of the III-nitride heterostructures.

DOI: 10.1103/PhysRevMaterials.6.044602

I. INTRODUCTION

III-nitride materials have garnered considerable interest over the last few decades for their extensive applications in electronics and optoelectronics, including laser diodes [1] for automotive lighting [2], solid-state lighting [3], and communications [4] as well as light-emitting diodes (LEDs) [5] for general lighting [3,6], displays [7], and visible-light communication (VLC) [8–10] technologies. Typical InGaN-based LED designs consist of active regions with one or more InGaN quantum wells (QWs), utilizing the narrower bandgap of InGaN (where the emission color can be tuned by adjusting the In content) compared to GaN to ensure carrier confinement and facilitate recombination between the electrons and holes. Another application of III-nitride materials in the field of optoelectronics is in photovoltaic cells [11], due to the wide tunability of the bandgap to access the full solar spectrum in multijunction solar cells. Despite the wealth of research in the field of III-nitride devices, the details of carrier transport within QW active regions remains poorly understood.

To study carrier transport, unipolar heterostructures have been used as test vehicles for theoretical models as they are

only subject to carrier transport behavior, circumventing the need to account for radiative and nonradiative recombination behavior. This approach was first proposed by Browne *et al.* [12] for the case of electron transport in InGaN using unipolar *n*-type GaN/InGaN/GaN heterostructures grown by ammonia-assisted molecular beam epitaxy (NH₃-MBE) and metalorganic chemical vapor deposition (MOCVD). The results indicated that even a 3-nm-thick In_{0.13}Ga_{0.87}N layer would act as a barrier to electron transport [12]. The notion of InGaN, which has a lower bandgap than GaN, as a barrier may seem counterintuitive at first glance, but can be explained using the concept of polarization fields. III-nitride heterostructures, such as InGaN/GaN, feature piezoelectric as well as spontaneous polarization fields [13]. Due to the difference in lattice constants between GaN and InGaN materials, the compressive strain affects the piezoelectric component of the polarization, causing significant polarization discontinuity between GaN and InGaN layers. The polarization discontinuity results in the formation of a polarization-induced charge at the interface between GaN and InGaN, with holes accumulating on the bottom interface and with ionized acceptors (N_A^-) on the top (assuming the structure is c-plane). Thus, an electric field forms at both interfaces, which in turn induces large band bending in the region, forming a barrier against both electron and hole transport, as shown in Fig. 1 [14].

Previous studies focused solely on the electron transport mechanism and is not applicable when discussing the

*These authors contributed equally to this work.

†Corresponding author: claytonqwah@gmail.com

‡Corresponding author: mmonavarian@ucsb.edu

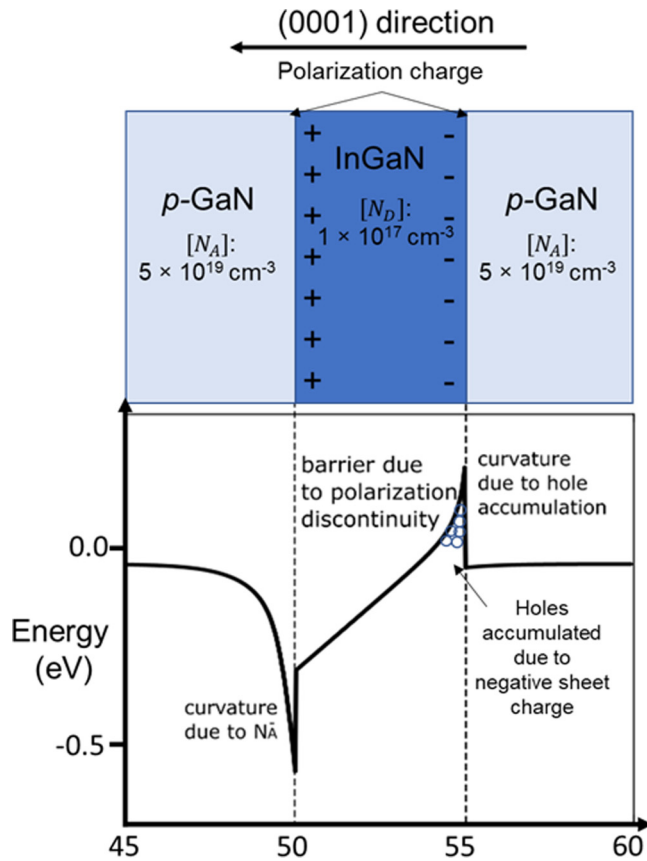


FIG. 1. Diagram detailing the sheet charge due to polarization discontinuities and the resultant valence band profile. The hole accumulation causes band curvature on the right of the QW and the ionized acceptors (N_A^-) on the left.

physics of hole transport (due to their different effective masses and conduction-versus-valence band offset), which is of great interest in the field of electronics and optoelectronics. With regard to hole transport structures, we [15] demonstrated electrical measurements on p -type unipolar AlGaIn heterostructures, which were enabled by n -to- p tunnel junctions (TJs). The results indicated that unintentionally doped (UID) AlGaIn can act as a barrier to hole transport and that a moderate p -type doping of the AlGaIn layer could suppress the barrier to hole injection, indicating the necessity of doping the AlGaIn electron-blocking layer for efficient hole injection in LED structures.

In this paper, we report the computational and experimental investigation of vertical hole transport through InGaIn layers in p -type unipolar heterostructures. The transport behavior is expected to be different for InGaIn compared to AlGaIn due to their different bandgaps and the corresponding band structures. For theoretical calculations, a computational model using standard drift-diffusion formalism that incorporates Localization Landscape theory, both in one and three dimensions are used. Our three-dimensional (3D) calculations also consider the effects of random alloy fluctuations within the InGaIn region to simulate the disordered potential that carriers are exposed to see when transporting through the structure. To support the device simulations, unipolar p -

type vertical transport structures are grown using NH_3 -MBE, with the unipolar InGaIn regions sitting on top of an n -to- p TJ. The tunnel junction layer is pivotal for our vertical transport structure as it helps with current spreading, due to the high resistivity of the p -GaIn material. This could potentially cause the current to go through the sidewalls of the mesa structures instead of the InGaIn layer. Apart from that, exposure of the p -GaIn layer to ion damage during the reactive-ion etch process could cause material damage, generating nitrogen vacancies [16] that act as shallow donors, which behave as compensating defects [17]. The experimental and computational data indicate an existence of barriers to hole transport through UID InGaIn double heterostructures (DHs) and quantum wells (QWs) in both reverse and forward bias.

Traditional 1D simulation packages, which use Schrödinger-Poisson-drift-diffusion calculations, consistently overestimate the turn-on voltage in LEDs. This is due to the assumption of abrupt junctions between GaIn and InGaIn as well as uniform alloy composition within the QWs [18]. However, incorporating the random alloy requires a huge amount of mesh nodes, which in turn requires an excessive amount of time to solve for the eigenstates due to the complexity of accounting for alloy disorder [18]. Hence, a new theory called Localization Landscape theory was proposed to solve the effective quantum potential without solving the eigenvalue problem. This theory was initially used to solve for systems with Anderson localization [19]. It can be included in Poisson and drift-diffusion solvers for modeling the carrier transport and recombination characteristics within LEDs [18,20]. Li *et. al* [18] estimated a significant reduction (nearly three orders of magnitude) in computation time when using the Localization Landscape theory compared to regular Schrödinger-Poisson methods for solving for disordered potentials.

II. SIMULATION PROCEDURE

The band diagrams and current density-voltage (J - V) simulations were obtained by conducting Poisson-drift-diffusion calculations. The algorithm used by the software is the Gummel iteration method (Fig. 2), which is a widely used algorithm used for solving for band energies as well as J - V characteristics [21]. In addition, the software also uses Localization Landscape theory [18], whereby instead of solving the time-independent Schrödinger eigen equation

$$\hat{H}\psi = \hat{E}\psi, \quad (1)$$

it solves an ordinary differential equation

$$\hat{H}u = 1, \quad (2)$$

where \hat{H} is the Hamiltonian operator:

$$\hat{H} = -\hbar^2 \nabla^2 \left(\frac{1}{2m^*} \nabla \right) + E_{c,v}. \quad (3)$$

ψ is the eigenfunction for the Hamiltonian operator and u is the landscape function.

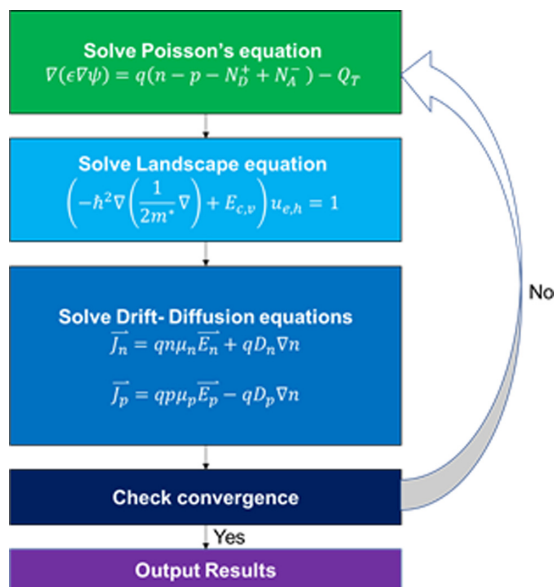


FIG. 2. Flow chart for the Gummel Method, which details the Poisson-drift-diffusion calculations as well as incorporates the Localization Landscape theory.

The theory posits that the locations of eigenstates, ψ in a specified potential V can be predicted using the solution of the equation, u . This is done by defining an effective potential called the Landscape potential, W , where $W = 1/u$. It was shown that W delimits the regions where the eigenstates are located [14]. Thus, the landscape potential can be seen as an effective confining potential that partitions a system into subregions where low-energy eigenstate are localized. The original eigenfunction, ψ , is recovered from both W and u via an auxiliary function described in [22], thus showing that they are intrinsically connected to the Schrödinger equation.

To model the InGaN region of the structure, we have conducted both 1D and 3D simulations. The parameters of our simulations are tabulated on Table I and Table II. The 1D model assumes the InGaN alloy region to be homogeneously made of a semiconducting material that has properties that are interpolated between GaN and InN. This is unrealistic as actual alloys are not homogeneous, and have GaN and InN randomly distributed throughout the region. Thus, we decided to conduct a 3D simulation, which allows for the incorporation of these compositional fluctuations within the InGaN alloy. According to Browne *et al.* [12], these fluctuations were found to improve electron transport within the alloy material as they result in a locally varying strain profile, which in turn affects the strength of the piezoelectric polarization field. Thus, regions of lower indium composition would have lower barrier heights, facilitating the injection of electrons.

TABLE II. Bandgap, effective masses, relative permittivity, bowing parameter [24,25] and piezoelectric coefficient values [26] used[27] in the simulations for GaN and InN.

Units	GaN	InN
E_g (eV)	3.437	0.61
m_e^{\parallel} (m_0)	0.21	0.07
m_e^{\perp} (m_0)	0.2	0.07
m_{hh} (m_0)	1.87	1.61
m_{lh} (m_0)	0.14	0.11
ϵ_r	10.4	15.3
e_{33} ($\frac{C}{cm^2}$)	0.73	0.73
e_{31} ($\frac{C}{cm^2}$)	-0.49	-0.49
e_{15} ($\frac{C}{cm^2}$)	-0.40	-0.40
Bowing parameter	1.4	
Mass of electron, m_0 (kg)	9.11×10^{-31}	

These regions where electrons have a lower barrier have been dubbed “percolation pathways” by previous studies [15,23]. For the 3D simulations, a random In composition map with an average composition of choice ($\sim 10\%$) was used as one of the input parameters for the full 3D calculation. A cross-sectional view of the 3D simulated InGaN quantum wells and double heterostructures, with their corresponding schematic, were plotted and shown on Fig. 3.

The alloys are generated by constructing a grid of lattice sites, with a distance of 2.833 Å between sites, and with indium and gallium being randomly assigned to each site. Following this, a Gaussian broadening is conducted to smoothen the alloy disorder using the following equation:

$$x(r_i) = \frac{\sum_j \text{atom}(j) \times e^{-\frac{(r_j-r_i)^2}{2\sigma^2}}}{\sum_j e^{-\frac{(r_j-r_i)^2}{2\sigma^2}}}, \quad (4)$$

where x is the composition in the region, with the sum going over all atomic sites j of the domain. The $\text{atom}(j)$ is randomly decided to be either Ga or In, and σ is the half-width of the Gaussian broadening parameter. The value of this parameter was chosen to be $\sigma = 2a$ (≈ 0.6 nm). This was chosen based on the findings of Ref. [23], where they compared simulations with experimental atomic probe tomography (APT) data. In their work, APT data showed that the average indium composition along the quantum well had a full width at half maximum of 1.5 nm. This tallies with our choice of $\sigma = 2a$ for the Gaussian broadening width, 2σ . Since a is the lattice constant of GaN, which is 0.3186 nm, this means $2\sigma = 1.274$ nm, which is very close the FWHM value seen from the reference. This contrasts with the 1D simulations, which uses an average composition map with

TABLE I. Doping levels in each layer in the simulation and their activation energies.

Layer	p -GaN	UID-InGaN (n -type)	GaN quantum barriers (n -type)
Hole mobility (cm^2/Vs)	5	10	10
Doping (cm^{-3})	5×10^{19}	1×10^{17}	1×10^{17}
Activation energy (meV)	180 (Mg)	34 (O)	34 (O)

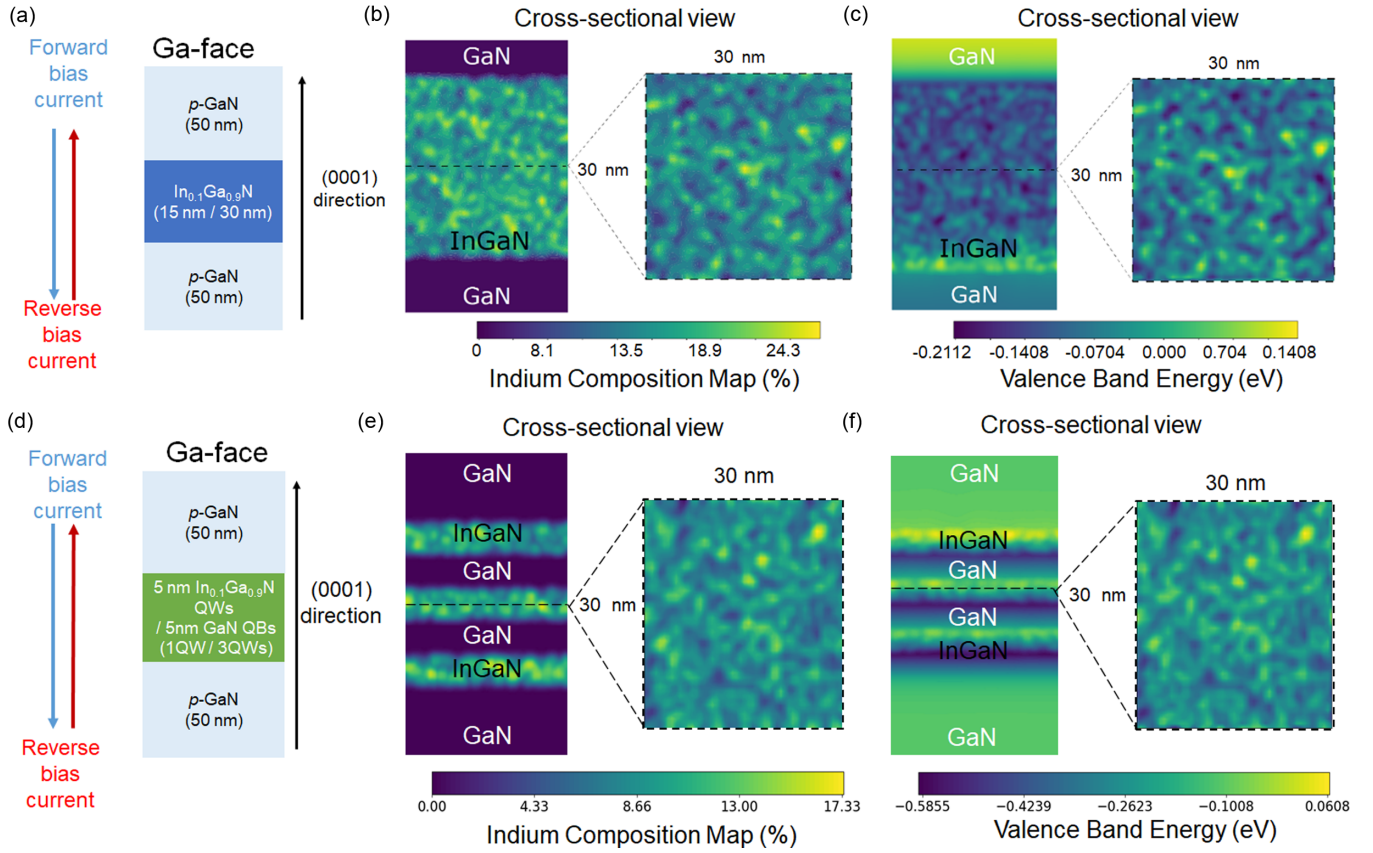


FIG. 3. Schematics of the simulated DH (a) and MQW(d) devices along with the growth polarity and directionality of forward bias and reverse bias current. Panels (b) and (c) show the resulting indium composition map and valence band energy map, respectively, for a 30-nm-thick InGaN structure. Panels (e) and (f) show the same maps for the 3×5 -nm MQW structure.

no random compositional fluctuations. The entire mesh is generated with a software called GMesh, with the equations being self-consistently solved over each node.

The conduction band (E_c) and valence band (E_v) energies are calculated by solving Poisson's equation. These energies are plugged into the landscape equation and then used to calculate landscape potential for electrons (W_e) and holes (W_h). Following that, they were then used to obtain electron and hole carrier densities by integrating the Fermi-Dirac distribution function over the energy bands using the following integrals:

$$n = \int_{W_e}^{\infty} \sqrt{|E - W_e|} \frac{\sqrt{2}m_n^{*3/2}}{\pi^2 \hbar^3} f_n(E) dE \quad (5)$$

and

$$p = \int_{-\infty}^{W_h} \sqrt{|W_h - E|} \frac{\sqrt{2}m_p^{*3/2}}{\pi^2 \hbar^3} f_p(E) dE, \quad (6)$$

where m_n^* , m_p^* , f_n , and f_p are the effective masses and Fermi-Dirac distribution functions for electrons and holes, respectively. The simulated temperature of the device is assumed to be 300 K. Since electrons are minority carriers in p -type unipolar structures, their effects are assumed to be negligible, and thus no appreciable recombination occurs within the structures.

III. SIMULATION RESULTS AND DISCUSSION

Band-diagram calculations are obtained for a 15-nm c -plane Ga-polar $\text{In}_{0.1}\text{Ga}_{0.9}\text{N}$ layer, as demonstrated in Fig. 4. The structures consist of the InGaN barrier layer sandwiched between Mg-doped p -GaN layers with a doping density of $5 \times 10^{19} \text{ cm}^{-3}$. Using the calculated band energies, estimated barrier heights for forward and reverse bias are indicated by arrows in Fig. 4(b). Finally, J - V results were obtained for both 1D and 3D unipolar structures for InGaN DH layers of 15-nm and 30-nm thicknesses. In the context of our unipolar device, we have defined forward bias as injecting holes from the top contact toward the bottom contact and vice versa for reverse bias. The main takeaway from the band energy simulation results is that holes experience barriers that are asymmetric in forward and reverse biases, with the reverse bias case generating a larger barrier compared to the forward case. In either forward or reverse bias, the barrier to the hole transport becomes larger as the thickness of the InGaN layer is increased.

The quantified barrier heights for each bias were then plotted in Fig. 5(a). The barrier heights are quantified by subtracting the highest from the lowest valence band energies in the direction of hole transport, as shown in Fig. 4(a). The maximum calculated barrier height for the 15-nm and 30-nm InGaN DH structures were 0.40 eV and 0.45 eV, respectively. The barrier height-versus-bias voltage plot [Fig. 5(a)] is

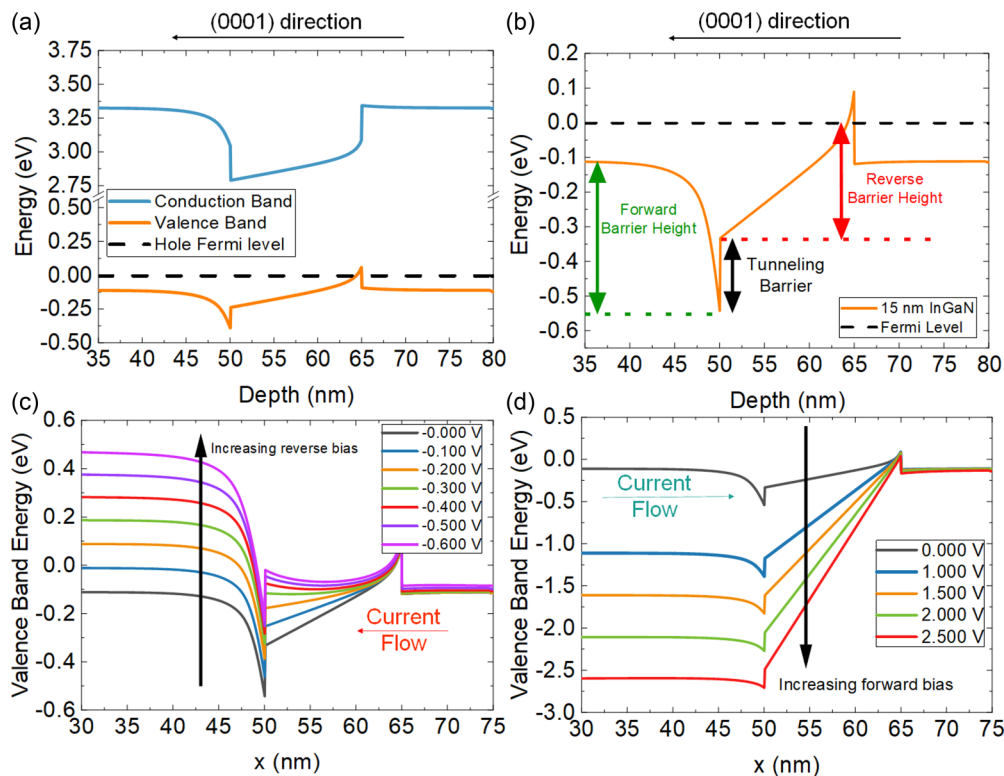


FIG. 4. (a) Full band diagram for the unipolar 15-nm InGaN DH structure. Valence band diagrams for *p*-type unipolar structures with a 15-nm layer of In_{0.1}Ga_{0.9}N at zero (b), reverse bias (c), and forward bias (d).

asymmetric with respect to the zero-bias point, as expected from the asymmetric band diagrams (Fig. 4) for the case of InGaN DHs. For example, the absolute barrier height to the hole transport at +1 V bias is higher compared to the barrier at -1 V (0.15 eV vs. 0.1 eV). The barrier asymmetry is also reflected in the simulated *J*-*V* data, where the voltages in the forward bias are much larger than those calculated in the reverse direction. For example, the voltage values at 100 A/cm² are significantly larger (1.2 V and 2.6 V for 15-nm and 30-nm InGaN DH layers in the 1D case, respectively) compared to those calculated at -100 A/cm² (~0.2 V for both the 15-nm and 30-nm DH InGaN layers in the 1D case), due to the asymmetry in the valence band diagrams (Fig. 4). In addition, the voltage drop for the 3D simulation is much lower compared to that of the 1D simulation, due to the percolative path-

ways associated with natural alloy fluctuations in the InGaN alloys. These percolative pathways form due to the random distribution of the two constituents in the alloys, which, because of their different band gaps, produces a corresponding random energy distribution in the band energies. Thus, the holes can traverse through the regions of low energies. The voltage values for the 3D simulations are almost negligible at -100 A/cm² for both barrier thicknesses, whereas the voltage at +100 A/cm² were at 0.05 V and 0.1 V for the 15-nm and 30-nm InGaN layers, respectively.

In addition to the InGaN DH structures, a similar analysis was conducted on single 5-nm and 3 × 5-nm multi-QW (MQW) structures with the same composition of indium (~0.1) (Figs. 6 and 7). In contrast to the InGaN DH layers, the MQW structure showed a more symmetric barrier height

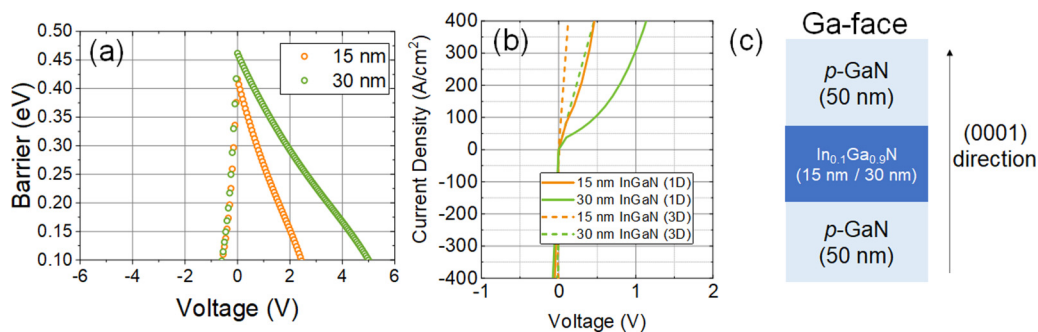


FIG. 5. (a) Estimated barrier height versus applied bias voltage to the structure for a 15-nm InGaN DH. The data show that the barrier height is lower in reverse compared to forward bias. (b) Comparison of simulated *J*-*V* results for 1D and 3D models for 15- and 30-nm-thick InGaN DH layers. (c) Schematic of the simulated structures.

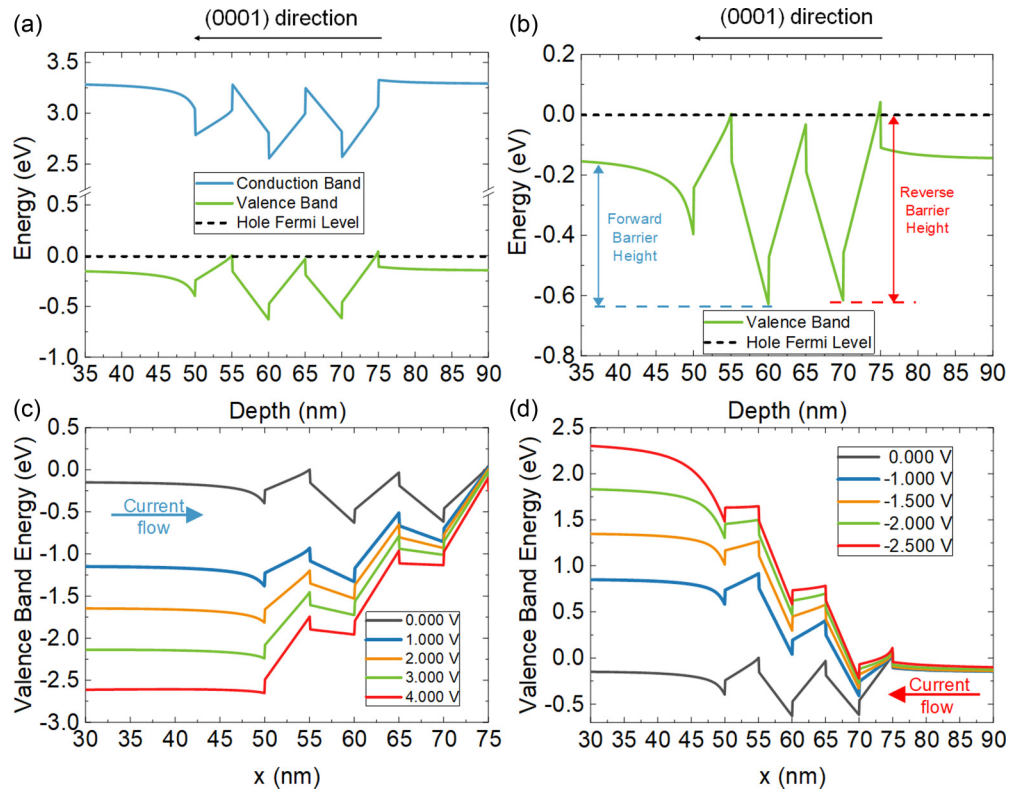


FIG. 6. (a) Full band diagram for a 3×5 -nm QW structure. Valence band diagrams for p -type unipolar structures with 3×5 -nm MQWs at zero (b), reverse bias (c) and forward bias (d).

in forward and reverse biases compared to the InGaN DHs, which is also reflected in the J - V simulations and the barrier height analysis [Fig. 7(a) and 7(b)]. The maximum calculated barrier heights for the single QW (SQW) and MQW structures were 0.35 eV and 0.50 eV, respectively. According to the J - V results, the MQW structure shows an increased voltage penalty compared to the SQW structure in both forward and reverse biases. Furthermore, the difference between the 1D and 3D J - V simulation results are much more significant for the case of a SQW compared to the MQW case. The results suggest that the hole transport is significantly hindered by the polarization barrier between the InGaN QW and GaN quantum barrier (QB) for the MQW structure. On the other hand, in the case of the SQW structure, the polarization barrier is

less pronounced, and so the presence of percolative pathways for the holes will result in significantly higher J at a given bias for a 3D model compared to the 1D case without alloy disorder.

IV. EXPERIMENTAL PROCEDURE

To verify experimentally the observed simulation results, unipolar hole transport structures with similar InGaN DH and QW structures were grown. Each structure consists of a unipolar p -type InGaN heterostructure on top of an n -to- p TJ. All structures were grown by NH_3 -MBE on a Veeco Gen 930 on 1 cm^2 MOCVD-grown GaN/Sapphire templates from Lumilog Saint-Gobain. Prior to growth, a Ti/Pd/Ti

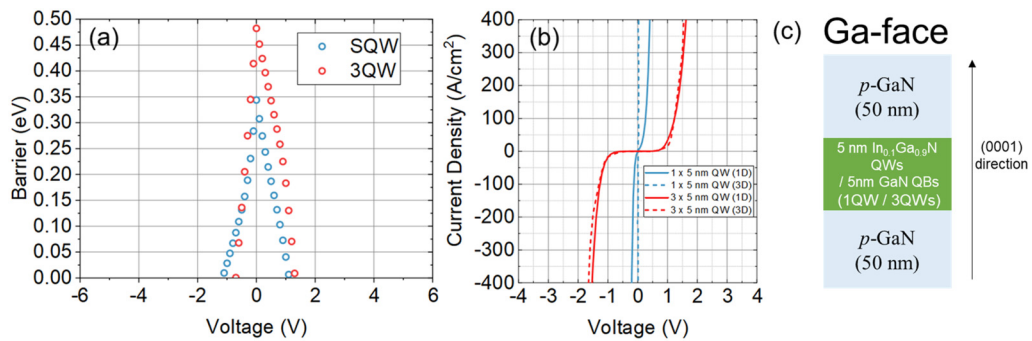


FIG. 7. (a) Estimated barrier heights versus applied bias to the MQW structure. Data show that the barrier height is lower in reverse compared to forward bias. (b) Comparison of 1D and 3D simulated J - V results for SQW and MQW structures. (c) Schematic of the simulated structures.

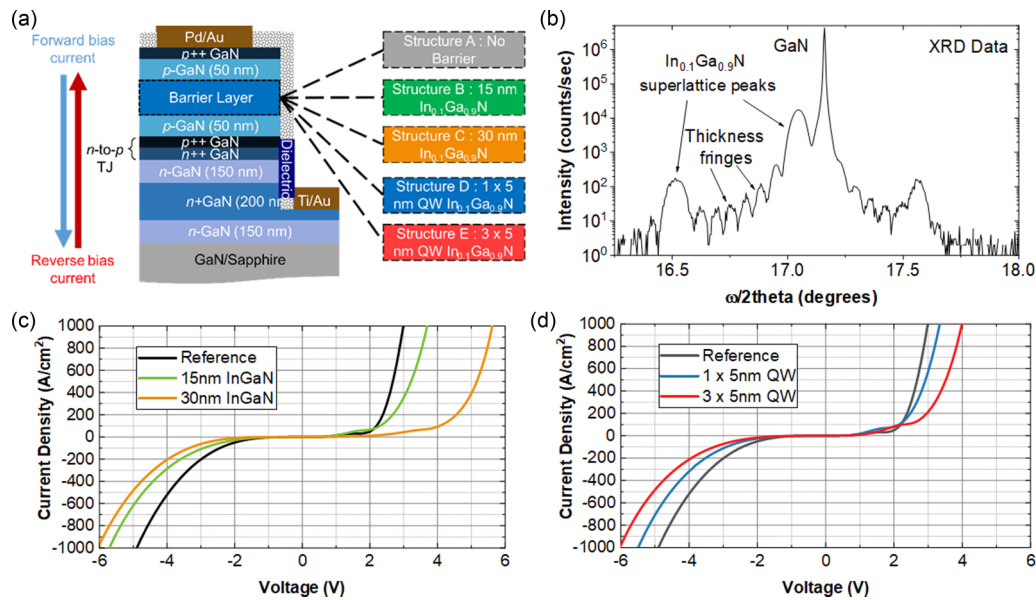


FIG. 8. (a) Schematic of all the structures grown and fabricated in this study. (b) HRXRD data of the calibration structure used for the $\text{In}_{0.1}\text{Ga}_{0.9}\text{N}$ structure. (c) Experimental J - V plots for the InGaN DH series. (d) Experimental J - V plots for the QW series. Panels (c) and (d) shows the J - V data for all the samples.

(50/500/100-nm) metal stack was deposited on the back of the samples to improve heat conduction from the heating filament to the substrates and to monitor surface temperature more accurately via an optical pyrometer. The samples were then cleaned using standard solvent cleaning procedures, which is immersing them in acetone, methanol, and isopropanol successively under sonication. The samples were then loaded into the system and baked at 400°C for an hour. Dual-filament effusion cells were used to supply elemental Ga and In for GaN and InGaN growth and for Mg and Si dopants for p -type and n -type doping, respectively. A showerhead injector was used to supply NH_3 , which provides the elemental N for growth. All growths were conducted under a 200-standard cubic centimeter NH_3 flow rate and a reactor pressure of 1×10^{-5} Torr. The growth structures consist of the following layers: first, an ~ 200 -nm-thick n + GaN contact layer ([Si]: $5 \times 10^{19} \text{cm}^{-3}$) was grown between two layers of 150-nm n -GaN ([Si]: $5 \times 10^{19} \text{cm}^{-3}$) at a substrate temperature of $\sim 820^\circ\text{C}$. Then, an n -to- p TJ was grown with a highly doped p^{++} ([Mg]: $5 \times 10^{20} \text{cm}^{-3}$)- n^{++} ([Si]: $5 \times 10^{20} \text{cm}^{-3}$) (10-nm/10-nm) design. The unipolar heterostructure was then separately grown, consisting of UID InGaN DH or QW layers sandwiched between two 50-nm-thick p -GaN ([Mg]: $5 \times 10^{19} \text{cm}^{-3}$) layers at a 750°C substrate temperature. The following structures were grown: sample A with no InGaN as a reference, sample B with a 15-nm UID $\text{In}_{0.1}\text{Ga}_{0.9}\text{N}$ DH layer, sample C with a 30-nm UID $\text{In}_{0.1}\text{Ga}_{0.9}\text{N}$ DH layer, sample D with 1×5 -nm UID $\text{In}_{0.1}\text{Ga}_{0.9}\text{N}$ (SQW), and sample E with 3×5 -nm UID $\text{In}_{0.1}\text{Ga}_{0.9}\text{N}$ (MQW). In our previous investigation [15], we concluded that having an UID GaN as the barrier layer does not provide any significant barrier to the hole transport, so we excluded that particular structure in this investigation. Finally, the samples are capped with a 10-nm-thick p^{++} GaN ([Mg]: 3×10^{20}) contact layer. Thickness and composition calibrations were conducted on separately grown

calibration structures using high-resolution x-ray diffraction (HRXRD), while doping calibrations were conducted using secondary-ion mass spectroscopy on separately grown calibration samples.

The samples were then fabricated into standard mesa isolated devices with circular patterns. First, a SiO_2 layer (~ 300 nm) was deposited using plasma-enhanced chemical vapor deposition to protect the p^{++} GaN contact layers during the nanofabrication process. The mesas were then formed using self-aligned wet etching of SiO_2 with buffered hydrofluoric acid followed by a 400-nm dry etch using a reactive-ion etching system. After that, another SiO_2 layer was deposited by electron-beam deposition for the n - and p -contacts. The circular metal contacts that were deposited on the mesa had diameters of $50 \mu\text{m}$, $75 \mu\text{m}$, $100 \mu\text{m}$, $125 \mu\text{m}$, $150 \mu\text{m}$, $175 \mu\text{m}$, and $200 \mu\text{m}$. Finally, a probe station with tungsten probes connected to a Keithley 4200A-SCS Parameter Analyzer was used to measure the electrical characteristics of our structures. Since the vertical distance of the p -region is much smaller than the lateral dimensions, there should be little to no current crowding on the mesa sidewalls, and the current should be spread evenly through the mesas. Therefore, the current density, J , is simply the injected current divided by the area of the p -contacts.

V. EXPERIMENTAL RESULTS AND DISCUSSION

As shown in Fig. 8, strong correlations can be drawn between experimental and computational data. First, there is a larger voltage drop for the 30-nm-thick versus the 15-nm-thick InGaN DH layers. For the QW series, the trend is confirmed; the MQW structure shows a larger voltage drop compared to the SQW structure. Furthermore, the voltage drop in the forward bias is larger than in the reverse for the InGaN DH J - V data, particularly in the case of the thicker

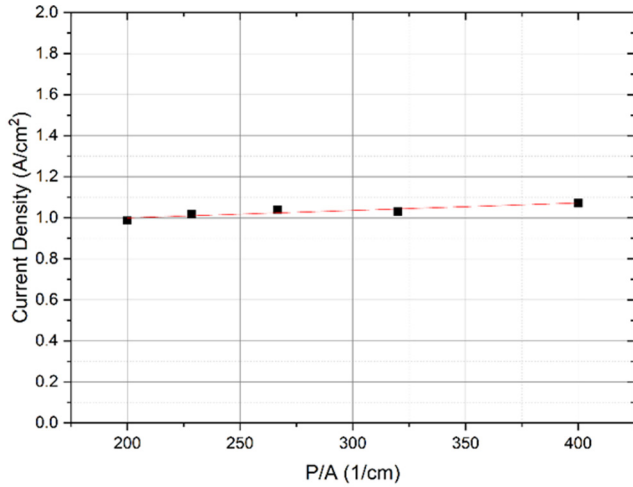


FIG. 9. Measured J as a function of the perimeter/area ratio (P/A). The dashed red line indicates a linear fitting of the data.

30-nm InGaN structure, where the voltage penalty was 2.25 V at 500 A/cm² compared to 1.25 V at -500 A/cm². The experimental data also confirm that in the case of the QW structures, the voltage penalty is more symmetric (~ 0.75 V at 500 A/cm² and ~ 1.0 V at -500 A/cm² for the MQW structure) compared to the InGaN DH series (~ 2.5 V at 500 A/cm² and ~ 1.0 V at -500 A/cm² for the 30-nm-thick InGaN DHs). At the low-voltage regime, the voltages are slightly higher in the reference sample compared to the transport structures, which is likely due to some variations between the samples in terms of contact resistivity and the doping in the TJs, which could result in slight variations in the J - V characteristics. We have also conducted a perimeter-to-area ratio analysis to determine the effect of sidewall leakage on the overall current density in our experimental results.

The voltages on all the structures are larger than those from the simulations, potentially due to the voltage penalty associated with the TJs and the contacts, which are not included in the simulations. Despite the inconsistency in the actual values of the voltages, the experimental results agree with the trend shown in our simulations, as adding the thickness and the

number of quantum wells does produce a larger barrier to hole transport. A significant factor that leads to the discrepancy is the inability of our models to account for tunneling behavior. Hence, we only consider transport through p - i - p layers, leading to a smaller voltage drop. Most TJ models today rely on the Wentzel-Kramer-Brillouin approximation [14], which is insufficient when accounting for tail states. In addition, most models today focus on the weak forward bias regime that was developed for narrow-bandgap semiconductors such as Si and GaAs [28,29]. For wide bandgap semiconductors such as GaN, the situation is more complicated due to the existence of the various defect states within the bandgap and the tail states. A consistent approach toward modeling the TJs is a subject of our other investigations, which will be published elsewhere.

Upon further inspection of the data, it is concluded that there is a dependence of the current density, J , on the device perimeter. The analysis was done using

$$J_{\text{Measured}} = \text{Area} \times J_{\text{Bulk}} + \text{Perimeter} \times J_{\text{perimeter}}.$$

Upon rearranging the terms, we obtain

$$J_{\text{Measured}} = \frac{\text{Perimeter}}{\text{Area}} \times J_{\text{perimeter}} + J_{\text{Bulk}}.$$

Thus, the measured current density (Fig. 9) at a given voltage for the different mesa sizes (i.e., their corresponding perimeter-to-area ratio) was plotted, as shown in Fig. 9. The data are also fitted linearly to obtain both the perimeter-dependent J from the slope as well as the corresponding bulk J from the y -intercept, which represents the true J - V characteristic, independent of the mesa size. The contribution of the perimeter term of J , $J_{\text{perimeter}}$ to the overall measured J obtained by dividing $J_{\text{perimeter}}$ by J_{Measured} for the device of size 200 μm was also plotted and is shown in Fig. 10(a).

As shown in Fig. 10 for the 200- μm device, $\sim 40\%$ of the current is from the outer section of the device. We attributed this to ion etch damage that must have seeped into the tunnel junction while processing the sample into devices. However, a plot of the bulk current density, J_{Bulk} , shows that the trend does exist and that InGaN acts a barrier to hole transport.

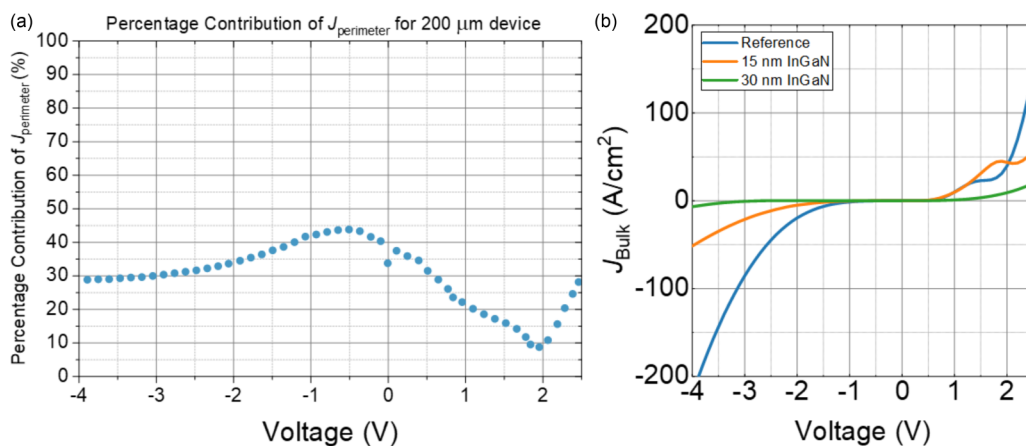


FIG. 10. (a) Percentage contribution of $J_{\text{perimeter}}$ on the overall current density for a 200- μm device. (b) Corrected J - V plots for the reference, 15-nm InGaN, and 30-nm InGaN samples, taking into account J_{Bulk} instead of J_{Measured} .

In conclusion, we investigated hole transport within InGaN alloys in p -type unipolar heterostructures through modeling and experimentation. Even a layer as thin as 5 nm of $\text{In}_{0.1}\text{Ga}_{0.9}\text{N}$ was sufficient to act as a barrier to hole transport in both reverse and forward bias. It was also found that, through the comparison of 1D and 3D simulations, percolative transport plays a larger role for the InGaN DH devices compared to the three-QW devices. This is believed to be due to the polarization discontinuity between the GaN layers and the InGaN QW layers, which hinders the transport of holes through the QW region. These findings will be important in our understanding of hole transport physics within GaN optoelectronics. Our results cement the effectiveness of unipolar hole transport structures, which are enabled by n -to- p TJs, as test vehicles for determining the barriers to hole transport. By decoupling recombination from the transport behavior, we can determine the validity of our simulations without the

complexities of recombination, which remains a challenge to simulate due to variation in recombination models.

ACKNOWLEDGMENTS

This work was supported by Collaborative Research in Engineering, Science and Technology (CREST), the Simons Foundation (Grant No. 601952, J.S.), Air Force Office of Scientific Research (Program No. FA9550-19-1-10090), National Science Foundation (NSF) RAISE program (Grant No. A007231601), Sandia National Laboratory (Award No. 2150283), and the Ministry of Science and Technology, Taiwan (Grant Nos. MOST 108-2628-E-002-010-MY3 and MOST 110-2923-E-002 -002). A portion of this work was performed at the University of California at Santa Barbara California NanoSystems Institute nanofabrication facility.

-
- [1] S. Nakamura, M. Senoh, S. Nagahama, N. Iwasa, T. Yamada, T. Matsushita, H. Kiyoku, and Y. Sugimoto, InGaN-based multi-quantum-well-structure laser diodes, *Jpn. J. Appl. Phys.* **35**, L74 (1996).
- [2] J. Hager, M. Seitz, C. Bemmer, P. Jahn, P. Ansorg, O. Woisetschläger, F. Buchmann, D. Sprenger, M. Vogl, O. Hering, J. Artzner, M. Glück, B. Reisinger, T. Mitterlehner, P. Schantl, L. Weber, S. Berlitz, and C. Neumann, Handling 17W of scanning laser power three years of exploration in the ILaS Project, in *Proceedings of the 12th International Symposium on Automotive Lightning* (Utz Verlag GmbH, München, Germany, 2017), p. 271.
- [3] S. P. DenBaars, D. Feezell, K. Kelchner, S. Pimputkar, C.-C. Pan, C.-C. Yen, S. Tanaka, Y. Zhao, N. Pfaff, R. Farrell, M. Iza, S. Keller, U. Mishra, J. S. Speck, and S. Nakamura, Development of gallium-nitride-based light-emitting diodes (LEDs) and laser diodes for energy-efficient lighting and displays, *Acta Mater.* **61**, 945 (2013).
- [4] S. Watson, S. Gwyn, S. Viola, G. Giuliano, T. J. Slight, S. Stanczyk, S. Grzanka, A. Yadav, D. Rowe, L. Laycock, K. E. Docherty, E. Rafailov, P. Perlin, S. Najda, M. Leszczynski, and A. E. Kelly, InGaN/GaN laser diodes and their applications, in *2018 20th International Conference on Transparent Optical Networks (ICTON)* (The Japan Society of Applied Physics, 2018), pp. 1.
- [5] S. Nakamura, M. Senoh, N. Iwasa, and S. Nagahama, High-brightness InGaN blue, green and yellow light-emitting diodes with quantum well structures, *Jpn. J. Appl. Phys.* **34**, L797 (1995).
- [6] D. Feezell and S. Nakamura, Invention, development, and status of the blue light-emitting diode, the enabler of solid-state lighting, *C.R. Phys.* **19**, 113 (2018).
- [7] M. Nami, A. Rashidi, M. Monavarian, S. Mishkat-Ul-Masabih, A. K. Rishinaramangalam, S. R. J. Brueck, and D. Feezell, Electrically injected GHz-class GaN/InGaN core-shell nanowire-based μ LEDs: carrier dynamics and nanoscale homogeneity, *ACS Photonics* **6**, 1618 (2019).
- [8] M. Monavarian, A. Rashidi, and D. Feezell, A decade of nonpolar and semipolar III-nitrides: A review of successes and challenges, *Physica Status Solidi (a)* **216**, 1800628 (2019).
- [9] S. Rajbhandari, J. J. D. McKendry, J. Herrnsdorf, H. Chun, G. Faulkner, Harald Haas, I. M. Watson, D. O'Brien, and M. D. Dawson, A review of gallium nitride LEDs for multi-gigabit-per-second visible light data communications, *Semicond. Sci. Technol.* **32**, 023001 (2017).
- [10] Y. D. Zhou, C. H. Chen, R. W. Chuang, S. J. Chang, Y. K. Su, P. C. Chang, P. C. Chen, H. Hung, S. M. Wang, and C. L. Yu, Nitride-based light emitting diode and photodetector dual function devices with InGaN/GaN multiple quantum well structures, *Solid State Electron.* **49**, 1347 (2005).
- [11] J. Wu, W. Walukiewicz, K. M. Yu, W. Shan, J. W. Ager, E. E. Haller, H. Lu, W. J. Schaff, W. K. Metzger, and S. Kurtz, Superior radiation resistance of $\text{In}_{1-x}\text{Ga}_x\text{N}$ alloys: full-solar-spectrum photovoltaic material system, *J. Appl. Phys.* **94**, 6477 (2003).
- [12] D. A. Browne, B. Mazumder, Y.-R. Wu, and J. S. Speck, Electron transport in unipolar InGaN/GaN multiple quantum well structures grown by NH_3 molecular beam epitaxy, *J. Appl. Phys.* **117**, 185703 (2015).
- [13] F. Bernardini, V. Fiorentini, and D. Vanderbilt, Spontaneous polarization and piezoelectric constants of III-V nitrides, *Phys. Rev. B* **56**, R10024 (1997).
- [14] S. Krishnamoorthy, D. N. Nath, F. Akyol, P. S. Park, M. Esposito, and S. Rajan, Polarization-engineered GaN/InGaN/GaN tunnel diodes, *Appl. Phys. Lett.* **97**, 203502 (2010).
- [15] K. S. Qwah, M. Monavarian, G. Lheureux, J. Wang, Y.-R. Wu, and J. S. Speck, Theoretical and experimental investigations of vertical hole transport through unipolar AlGaIn structures: impacts of random alloy disorder, *Appl. Phys. Lett.* **117**, 022107 (2020).
- [16] X. A. Cao, H. Cho, S. J. Pearton, G. T. Dang, A. P. Zhang, F. Ren, R. J. Shul, L. Zhang, R. Hickman, and J. M. Van Hove,

- Depth and thermal stability of dry etch damage in GaN Schottky diodes, *Appl. Phys. Lett.* **75**, 232 (1999).
- [17] D. W. Jenkins and J. D. Dow, Electronic structures and doping of InN, $\text{In}_x\text{Ga}_{1-x}\text{N}$, and $\text{In}_x\text{Al}_{1-x}\text{N}$, *Phys. Rev. B* **39**, 3317 (1989).
- [18] C.-K. Li, M. Piccardo, L.-S. Lu, S. Mayboroda, L. Martinelli, J. Peretti, J. S. Speck, C. Weisbuch, M. Filoche, and Y.-R. Wu, Localization landscape theory of disorder in semiconductors: III. Application to carrier transport and recombination in light emitting diodes, *Phys. Rev. B* **95**, 144206 (2017).
- [19] M. Filoche and S. Mayboroda, Universal mechanism for Anderson and weak localization, *Proc. Natl. Acad. Sci. USA* **109**, 14761 (2012).
- [20] H.-H. Chen, J. S. Speck, C. Weisbuch, and Y.-R. Wu, Three dimensional simulation on the transport and quantum efficiency of UVC-LEDs with random alloy fluctuations, *Appl. Phys. Lett.* **113**, 153504 (2018).
- [21] H. K. Gummel, A self-consistent iterative scheme for one-dimensional steady state transistor calculations, *IEEE Trans. Electron Devices* **11**, 455 (1964).
- [22] D. N. Arnold, G. David, D. Jerison, S. Mayboroda, and M. Filoche, Effective Confining Potential of Quantum States in Disordered Media, *Phys. Rev. Lett.* **116**, 056602 (2016).
- [23] T.-J. Yang, R. Shivaraman, J. S. Speck, and Y.-R. Wu, The influence of random indium alloy fluctuations in indium gallium nitride quantum wells on the device behavior, *J. Appl. Phys.* **116**, 113104 (2014).
- [24] I. Vurgaftman, J. R. Meyer, and L. R. Ram-Mohan, Band parameters for III-V compound semiconductors and their alloys, *J. Appl. Phys.* **89**, 5815 (2001).
- [25] J. Piprek, *Nitride Semiconductor Devices: Principles and Simulation* (Wiley, Weinheim, Germany, 2007).
- [26] A. E. Romanov, T. J. Baker, S. Nakamura, and J. S. Speck, Strain-induced polarization in wurtzite III-nitride semipolar layers, *J. Appl. Phys.* **100**, 023522 (2006).
- [27] See Supplemental Material at <http://link.aps.org/supplemental/10.1103/PhysRevMaterials.6.044602> for the design of the mask used for lithography.
- [28] N. Moulin, M. Amara, F. Mandorlo, and M. Lemiti, Tunnel junction I(V) characteristics: review and a new model for p-n homojunctions, *J. Appl. Phys.* **126**, 033105 (2019).
- [29] M. Hermle, G. Létay, S. P. Philipps, and A. W. Bett, Numerical simulation of tunnel diodes for multi-junction solar cells, *Prog. Photovoltaics Res. Appl.* **16**, 409 (2008).